

A distribution-dependent Mumford-Shah model for unsupervised hyperspectral image segmentation

Jan-Christopher Cohrs, Chandrajit Bajaj, *Fellow, IEEE*, Benjamin Berkels

Abstract—Hyperspectral images provide a rich representation of the underlying spectrum for each pixel, allowing for a pixel-wise classification/segmentation into different classes. As the acquisition of labeled training data is very time-consuming, unsupervised methods become crucial in hyperspectral image analysis. The spectral variability and noise in hyperspectral data make this task very challenging and define special requirements for such methods.

Here, we present a novel unsupervised hyperspectral segmentation framework. It starts with a denoising and dimensionality reduction step by the well-established Minimum Noise Fraction (MNF) transform. Then, the Mumford-Shah (MS) segmentation functional is applied to segment the data. We equipped the MS functional with a novel robust distribution-dependent indicator function designed to handle the characteristic challenges of hyperspectral data. To optimize our objective function with respect to the parameters for which no closed form solution is available, we propose an efficient fixed point iteration scheme. Numerical experiments on four public benchmark datasets show that our method produces competitive results, which outperform two state-of-the-art methods substantially on three of these datasets.

Index Terms—Classification, hyperspectral imaging, Mumford-Shah, segmentation, spectral variability, total variation, unsupervised

I. INTRODUCTION

IN many research areas that are concerned with an image-based analysis of specimens or scenes, hyperspectral images are becoming more and more popular. Modern hyperspectral imaging (HSI) sensors sample the spectral space with a very high spectral resolution, resulting in very detailed and rich representations of the spectra at each pixel [1]. HSI is often applied in the field of remote sensing, where it is used in agriculture, mineralogy, surveillance and environmental management [2]. The sensors consider a large part of the electromagnetic spectrum. For instance, in the case of an Airborne visible/infrared imaging spectrometer (AVIRIS) the visible and infrared wavelengths are sampled with a very small step size [1]. However, HSI is also attracting more attention in areas like, e.g., biomedical imaging in the form of Fourier transform infrared spectrometry, which measures a large part of the infrared regime [3].

HSI assumes that constituents, like materials, that are present in a scene or specimen reflect specific wavelengths,

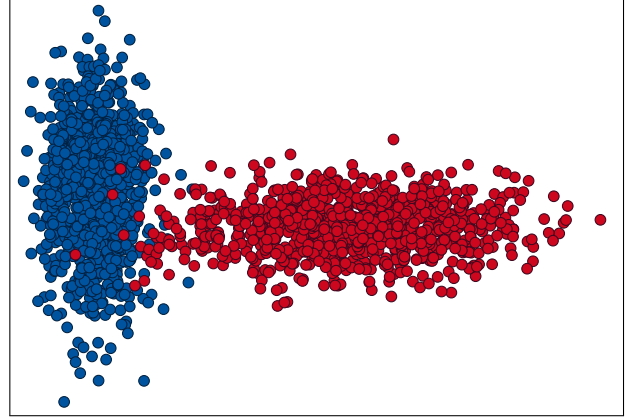


Figure 1: Toy example of an image with two segments and two channels showing strong *spectral variability*. Each dot corresponds to a spectrum. The spectra were drawn from two different distributions and are shown in blue and red, respectively. Each distribution (or cluster) represents the recorded spectra that are variations of the spectral signature of one specific constituent. One can see that for both clusters the deviation around the mean spectrum differs in different directions. Although the toy example shows clusters that follow a Gaussian distribution by design, the clusters can follow any distribution in general.

which can be seen as *spectral signatures* of these constituents [1]. In particular, this allows for a pixel-wise classification of an image into different constituent classes, if the spatial resolution is sufficiently small. Many spectrometers used in remote sensing do not fulfill this requirement as their spatial resolution is rather large. Consequently, *mixed pixels* are recorded that show a mixture of spectral signatures [1], which makes it harder to distinguish between the contributing constituents. In fact, *hyperspectral unmixing* focusses on this aspect of hyperspectral data and models each pixel as a mixture of a fixed number of discrete spectral signatures, called endmembers, with the goal to determine representations of the endmembers as well as the abundances [4]. Moreover, hyperspectral data often suffers from noise, which impedes the classification of the pixels further. The most challenging obstacle in HSI analysis, however, is the *spectral variability*. This phenomenon describes that within a constituent class the spectra show variations caused by changes in illumination conditions and material surfaces [5]. Fig. 1 shows a toy example of the spectral variability. Segmentation and classification methods have to take this effect into account when separating the

Jan-Christopher Cohrs and Benjamin Berkels are with the Aachen Institute for Advanced Study in Computational Engineering Science (AICES), RWTH Aachen University, Germany (email: cohres@aices.rwth-aachen.de; berkels@aices.rwth-aachen.de).

Chandrajit Bajaj is with the Oden Institute for Computational and Engineering Sciences, University of Texas at Austin, USA (email: bajaj@oden.utexas.edu).

clusters and classifying the pixels.

The problem of classifying pixels into segments or classes in the hyperspectral context is mainly tackled using supervised learning. Especially in the remote sensing community, this is a very active topic. There is a vast amount of literature on supervised approaches to classify hyperspectral images on a per pixel basis. Approaches that merely exploit spectral information are often based on support vector machines (SVMs) [6], [7]. Recent spectral-spatial approaches, i.e., combining spectral with spatial information, achieve generally higher scores than spectral approaches, because they exploit more information about the scene. These methods are mostly based on neural networks [8], [9], [10]. A serious shortcoming of supervised methods is the shortage of labeled data in the context of HSI that is needed to train the methods and obtain good generalization performance. In particular, current approaches typically train on a subset of the labeled pixels available for one image and test on the remaining labeled pixels of the very same image. Hence, a generalization of these approaches to new data cannot be expected. Generating labeled training data is very time-consuming. Furthermore, because only a limited number of training samples in a very high dimensional spectral space is available, the *Hughes phenomenon* [11] makes the classification more difficult. Unsupervised methods avoid these problems as they do not make use of any labeled data. The only prior knowledge that is incorporated is the number of segments that are sought. Some approaches even try to estimate the number of segments, but we will discuss in this article only methods that have this information. Richards and Jia differentiate between *a priori* labeling in the supervised and *a posteriori* labeling in the unsupervised setting [12]. The difference is that in the former case one needs a number of labeled training samples that have to be manually classified in advance, while in the latter case it is enough to take one sample from each class of interest after segmentation and assign a semantic label to the whole class with the support of spatial structures that the segmentation result provides. A posteriori labeling even allows for semantically labeling only those segments that are of interest, which reduces the need of manual input further.

There are only few works on unsupervised hyperspectral segmentation. Besides the known general clustering methods like, e.g., k -means, Gaussian mixture model and DBSCAN [13] that can be used for clustering of the spectra, there are some approaches tailored for HSI analysis. Zhu et al. [14] propose to combine a data fidelity term that is similar to the one in the MS segmentation model, as described below in Section II-A, with their developed nonlocal variant of the total variation semi-norm. Hassanzadeh et al. [15] introduce a new spectral clustering method, designed for large-scale HSI. The clustering is based on a bipartite graph representation with data affinity measured by the radial basis function kernel. A sequential singular value decomposition and mini-batch k -means are applied to find the segmentation. Zhang et al. [16] approach the problem by jointly reducing the dimensionality and performing the clustering using their developed unified low-rank matrix factorization. The idea is to decompose the data matrix into a product of a projection matrix and a

matrix containing lower dimensional representations of the data, while the representation matrix is further factorized into two matrices, one indicating the clusters and the other describing latent features.

Facing the aforementioned problems of supervised HSI classification and due to the advantages of unsupervised HSI segmentation, we present a novel unsupervised approach to HSI segmentation. Our method builds on the MS segmentation functional. We developed a new robust indicator function tailored for hyperspectral data that is able to handle spectral variability. It is a clustering method equipped with an anisotropic distribution-dependent distance function and a spectral cluster volume regularizer that is inspired by the normalization constant of the Gaussian distribution. Furthermore, with a second regularizer, we penalize large perimeters of segments. The motivating assumption for this is that neighboring pixels have a high probability to belong to the same segment. This introduces spatial information into the model only implicitly by considering the spatial gradient of the labeling function. Part of our framework is the application of the MNF transform to reduce the noise and dimensionality of the data. Only there we explicitly use spatial information when estimating the noise content by considering the differences of the pixels to their respective lower right neighbors. Hence, our framework is not a spectral approach; however, we want to point out that different from usual spectral-spatial approaches that process patches of pixels, our approach sees only a pixel plus one neighbor at a time.

The remaining article is structured as follows: Section II provides detailed information about our hyperspectral segmentation framework, i.e., the objective function of our method. Section III explains the optimization of our functional with an alternating optimization approach. Section IV shows our numerical results and Section V gives a conclusion of the article. The source code of our segmentation framework will be published upon acceptance.

II. METHODOLOGY

In the following, we give detailed information about our segmentation framework, starting with an explanation of the basic MS segmentation functional in Section II-A and then introducing our modification in Section II-B.

A. Mumford-Shah segmentation functional

We now describe the multi-phase MS segmentation functional [17] as the basis of our model. To this end, let $\Omega \subseteq \mathbb{R}^2$ be a domain, $k, \tilde{L} \in \mathbb{N}$ and $\tilde{g}: \Omega \rightarrow \tilde{V} \subseteq \mathbb{R}^{\tilde{L}}$ an input image. The MS segmentation functional is defined as

$$E_{\text{MS}}[\mathcal{O}_1, \dots, \mathcal{O}_k] = \sum_{l=1}^k \int_{\mathcal{O}_l} f_l(x) \, dx + \lambda \text{Per}(\mathcal{O}_l), \quad (1)$$

for a partition $(\mathcal{O}_1, \dots, \mathcal{O}_k)$ of the image domain Ω . The subsets $\mathcal{O}_1, \dots, \mathcal{O}_k$ describe the segments in the image. Our goal is to obtain a segmentation of the image by finding minimizers of the MS functional.

The functional consists of two parts: a data fidelity term, which is the integrals over the subsets of Ω , and a regularization term, which is the second summand in Eq. (1). The essential part of the data term is the so-called indicator functions $f_l: \Omega \rightarrow \mathbb{R}$ that measure how well $x \in \Omega$ fits into the respective segment \mathcal{O}_l . They are required to be bounded from below. These functions define the notion of homogeneity for the segments and are therefore playing a crucial role in the MS functional. By integrating the indicator functions and summing over all segments $\mathcal{O}_1, \dots, \mathcal{O}_k$, we obtain a measure of the goodness of a partition with respect to the chosen indicator functions. The regularizing term deals with the perimeters of the segments and penalizes these if they become too large. This term incorporates the spatial relations that are given by the image domain Ω . The underlying assumption is that neighboring positions in the image domain have a high probability to belong to the same segment. In particular, isolated points of a segment contribute to its perimeter and shall be avoided by this regularization, resulting in segmentations showing homogeneous regions. The hyperparameter $\lambda > 0$ balances the two terms in the functional.

In our case, the data term is taking care of the spectral information during segmentation. Since we assume that each material reflects a specific spectral signature (cf. Section I), we rely only on the spectral information when clustering the spectra and performing the segmentation. Hence, the indicator functions define the notion of spectral homogeneity in our case and should therefore respect the special characteristics of hyperspectral data. Our proposed indicator function is introduced in Section II-B.

To approximate minimizers of our objective function, we use Zach's convexification [18] of the MS functional. It is given as

$$J_{\text{Zach}}[u] = \sum_{l=1}^k \int_{\Omega} u_l(x) f_l(x) dx + \lambda |u_l|_{\text{BV}}, \quad (2)$$

where $u = (u_1, u_2, \dots, u_k): \Omega \rightarrow \mathbb{K}^k$ is the so-called *labeling function* that maps a point $x \in \Omega$ to the unit simplex in \mathbb{R}^k given as $\mathbb{K}^k = \{(s_1, s_2, \dots, s_k) \in \mathbb{R}^k \mid s_l \geq 0 \ \forall l \in \{1, \dots, k\}, \sum_{l=1}^k s_l = 1\}$. To derive Eq. (2) from Eq. (1), one introduces characteristic functions $\chi_{\mathcal{O}_l}(x)$ for \mathcal{O}_l in the integrals in Eq. (1). Then, the integrals can be extended to integrate over the whole image domain Ω . Relaxing the characteristic functions by replacing them by functions $u_l: \Omega \rightarrow [0, 1]$ such that $\sum_{l=1}^k u_l(x) = 1$ for every $x \in \Omega$ yields Eq. (2). The last term in Eq. (2) is a consequence of the relation $\text{Per}(\mathcal{O}_l) = |\chi_{\mathcal{O}_l}|_{\text{BV}}$, where $|\cdot|_{\text{BV}}$ is the bounded variation (BV) semi-norm, also known as total variation (TV).

B. Robust anisotropic indicator function

As already mentioned in Section II-A, one of the essential parts of the functional in Eq. (1) is the used indicator functions f_l that define the notion of spectral homogeneity and therefore the distance in spectral space. In the following, we describe our indicator function, designed to appropriately handle the characteristics of hyperspectral data. To this end, we consider the discrete setting, i.e., for a regular grid $\mathcal{N} =$

$\{1, 2, \dots, H\} \times \{1, 2, \dots, W\} \subseteq \mathbb{R}^2$, we consider an image $\tilde{g}: \mathcal{N} \rightarrow \tilde{V} \subseteq \mathbb{R}^{\tilde{L}}$ as well as indicator functions $f_l: \mathcal{N} \rightarrow \mathbb{R}$ for $l \in \{1, \dots, k\}$ that are bounded from below and a labeling function $u = (u_1, u_2, \dots, u_k): \mathcal{N} \rightarrow \mathbb{K}^k$.

The main challenge of hyperspectral data is, as mentioned in Section I and depicted in Fig. 1, the spectral variability. Since this means that variation of the data in some directions in spectral space is stronger than in others, the Euclidean norm as the classic choice for the indicator function is not sophisticated enough as it is isotropic, meaning that it assumes the same variation in each direction. Our indicator function generalizes the Euclidean norm by respecting the different strengths of variation for the respective directions and hence making it anisotropic and variability-dependent. To this end, we consider first and second order statistics of the current segment estimates and assume that the feature distributions of the segments follow approximately Gaussian distributions.

Before we apply our indicator function to the input image, we first input the image in the MNF transform. This step reduces the dimensionality of and noise in the data. Most importantly, it manipulates the data such that the feature distributions are more similar to Gaussian distributions making our assumption more suitable. Therefore, we now describe the MNF transform in Section II-B1 before we define and explain our indicator function in Section II-B2.

1) *MNF transform:* We use the MNF transform [19] as a step to reduce the noise as well as the dimensionality of the image \tilde{g} . The MNF is related to the often used Principal Components Analysis (PCA) [20]. But instead of returning components ordered by their explained variance as the PCA, it returns components ordered by their signal-to-noise ratio (SNR). To find the components that maximize the SNR, the MNF transform assumes additive noise, i.e., that the data fulfills

$$\tilde{g} = s + n,$$

where $s: \mathcal{N} \rightarrow \mathbb{R}^{\tilde{L}}$ is the true signal and $n: \mathcal{N} \rightarrow \mathbb{R}^{\tilde{L}}$ is the noise component. It is further supposed that the signal and noise are uncorrelated. Consequently, we obtain

$$\Sigma_D = \Sigma_S + \Sigma_N,$$

with $\Sigma_D \in \mathbb{R}^{\tilde{L} \times \tilde{L}}$ being the covariance matrix of the data and $\Sigma_S \in \mathbb{R}^{\tilde{L} \times \tilde{L}}$ and $\Sigma_N \in \mathbb{R}^{\tilde{L} \times \tilde{L}}$ the covariance matrices of the signal and the noise, respectively. The MNF transform simultaneously diagonalizes Σ_S and Σ_N

$$W^T \Sigma_S W = \Lambda, \quad W^T \Sigma_N W = I,$$

to obtain a basis of generalized eigenvectors $W \in \mathbb{R}^{\tilde{L} \times \tilde{L}}$, which are the sought components, and the generalized eigenvalues given on the diagonal of the diagonal matrix $\Lambda \in \mathbb{R}^{\tilde{L} \times \tilde{L}}$, which are the SNRs corresponding to the components [21]. The noise covariance matrix is transformed to the identity matrix as this decorrelates the noise between the bands and normalizes the noise in each band to 1 [22]. Hence, the i -th entry on the diagonal of Λ corresponds to the SNR of the i -th component (eigenvector) for $i \in \{1, \dots, \tilde{L}\}$. By keeping only $L \in \mathbb{N}$ with $L \leq \tilde{L}$ components that show a high SNR, we

reduce the dimensionality and the noise in the data at the same time. We denote the resulting image as

$$g: \mathcal{N} \rightarrow V \subseteq \mathbb{R}^L.$$

Different schemes to estimate the noise are possible. We use the difference of each pixel to its lower right neighbor based on the assumption that the true spectra are spatially constant. Of course, one could also consider the difference to a neighbor in another direction. All possible directions should give similar results. The obtained differences give a band-wise noise estimate for each pixel (except for pixels at the image boundaries) from which we can compute the global noise covariance matrix. In particular, by considering the neighboring relation of two pixels defined by \mathcal{N} , we take into account spatial relations of pixels here, which already helps to disentangle the spectral clusters slightly. A disadvantage of this noise estimation is that it is not informed about possible segment boundaries and hence considers the differences of the spectra at segment boundaries as noise and flattens these differences slightly, what results in a few spectra that lie between the spectral clusters. On the other hand, as described in [22], the MNF is equivalent to a two stage transformation that applies a data whitening step that transforms the noise covariance matrix to the identity matrix, followed by an application of the PCA. The data whitening makes the spectral clusters better fit the assumption of following approximately Gaussian distributions.

In cases where the size of the HSI data is very large, resulting in long runtimes of the MNF transform, more efficient variants of the transform might be considered to speed up computations. Three possible approaches are presented, for instance, in [23]. In cases where one deals with massive data, preventing the machine from processing the data at once and performing the MNF transform, one can use streaming models to process the data in chunks. One such approach is presented in [24].

2) *Definition of indicator function:* Let $g^{i,j} := g(i, j) \in V \subseteq \mathbb{R}^L$ for $(i, j) \in \mathcal{N}$. We define our indicator function for segment $l \in \{1, \dots, k\}$ as

$$f_l(i, j; \mu_l, \Sigma_l) := \sqrt{(g^{i,j} - \mu_l)^T \Sigma_l^{-1} (g^{i,j} - \mu_l)} + \log \det \Sigma_l, \quad (3)$$

where $\mu_l \in \mathbb{R}^L$ and $\Sigma_l \in \mathbb{R}^{L \times L}$ describe the current estimates of the mean spectrum and the covariance matrix of segment l , respectively. Note that the covariance matrix is symmetric by definition. Later in this section, we will describe how we regularize the covariance matrix to ensure that the used matrix in Eq. (3) is invertible. Our indicator function consists of two parts where the first summand computes the distribution-dependent distance of a spectrum $g^{i,j}$ to the mean spectrum of the segment and the second summand is a volume regularizer of the spectral cluster.

The key idea of the first term in Eq. (3) is to give a pixel a lower indicator value if it deviates from the mean spectrum of the segment in a direction where the feature distribution of the segment varies strongly and penalize small deviations in directions where the feature distribution has only a very small

standard deviation. By computing the eigendecomposition of the covariance matrix $\Sigma_l = U_l D_l^2 U_l^T$, where $U_l \in \mathbb{R}^{L \times L}$ is the orthogonal matrix containing the eigenvectors, which describe the principal directions of variation, and $D_l \in \mathbb{R}^{L \times L}$ is the diagonal matrix having the standard deviations $\sigma_{l,r} > 0$, $r \in \{1, \dots, L\}$, in the corresponding directions of variation on its diagonal, we can write Eq. (3) as

$$f_l(i, j; \mu_l, \Sigma_l) = \|D_l^{-1} U_l^T (g^{i,j} - \mu_l)\|_2 + \log \prod_{r=1}^L \sigma_{l,r}^2. \quad (4)$$

Eq. (4) allows for a geometric interpretation of the indicator function: we still measure the difference between the spectrum of the pixel at $(i, j) \in \mathcal{N}$ and the mean spectrum of the segment μ_l ; however, this difference is now projected onto the eigenvectors of Σ_l by the multiplication with U_l^T and scaled afterwards by the multiplication with the inverse of D_l . These two steps mean that the vector $g^{i,j} - \mu_l$ is scaled by $1/\sigma_{l,r}$ in the respective direction of the deviation. Hence, if the feature distribution of the segment deviates strongly in a certain direction, the standard deviation is large, implying that its reciprocal is small and resulting in a lower indicator value for that direction. If the feature distribution shows a very small deviation in a direction, the standard deviation is small, implying that its reciprocal is large what ends up in a large indicator value for that direction.

We propose further to use the square root in the indicator function in Eq. (3) to make the estimates of μ_l and Σ_l more robust against outliers. As already mentioned, hyperspectral data suffers from noise. Hence, due to the spectral variability and the noise, some spectra lie in the regions between clusters. Such spectra have a high potential to be misclassified with the result that they would negatively influence the estimates of μ_l and Σ_l . Moreover, the application of the MNF transform contributes to this effect, too, caused by the current simple approach to globally estimate the noise content based on differences of neighboring pixels (cf. Section II-B1). The problem is that pixels at segment boundaries contribute to the noise estimation for the MNF although their difference in the spectra stems from different constituents in the scene and is therefore natural, wanted and needed for the distinction of these constituents. In particular, the estimate of μ_l , for instance, may move away from the dense region of the feature distribution and towards the outliers. This effect is much weaker if we use the square root in Eq. (3) compared to the indicator function without square root. A downside of this idea is that, to the best of our knowledge, there exists no closed form solution for choices of μ_l and Σ_l that let the gradient vanish in order to optimize over these quantities. In Section III-B, we describe a simple fixed point iteration scheme to optimize over the two parameters. Please note that the distance term of Eq. (3) is, in fact, an instance of the Mahalanobis distance [25].

The second term in Eq. (3) is a spectral volume regularizer for each segment that tries to keep the cluster volumes small by minimizing the standard deviations. This helps to balance the regularizing perimeter and the data term in Eq. (1). By considering the spatial neighborhood relations the perimeter

makes it possible to put spatially close pixels into the same segment that are spectrally apart. However, doing so increases the cluster volumes and hence the standard deviations of the clusters, which makes deviations of spectra from the mean spectrum cheaper and can result in misclassifications. From an optimization perspective, it is cheapest to let the standard deviations tend to ∞ if the spectral volume regularizer was omitted. This would make the scaling factors of our indicator function tend to 0 and hence the data term could be made arbitrarily small with 0 as lower bound. By keeping the standard deviations of the clusters small, this effect is avoided. Please note that for fixed μ_l and Σ_l the volume regularizer is only a constant shift of the indicator function.

The similarity of our model to the Gaussian mixture model is clearly visible. Indeed, both models assume that the spectral clusters follow Gaussian distributions. However, there are some differences. Our model assumes that all clusters are equally likely. Moreover, since our model does not work with probability distributions, we have more flexibility regarding its design. It is therefore feasible to have the square root in the indicator function. Having this in a Gaussian distribution would make the integral over the full probability space diverge.

To deal with the occurrence of singular matrices D_l and Σ_l , we propose to regularize these matrices and use the resulting matrices in the framework. Concretely, we introduce a small $\epsilon > 0$ and replace $\sigma_{l,r}$ in D_l by ϵ if $\sigma_{l,r} \leq \epsilon$. We denote the arising regularized matrices with $D_{\epsilon,l}$ and $\Sigma_{\epsilon,l} = U_l D_{\epsilon,l}^2 U_l^T$ and define $\Sigma_{\epsilon} := (\Sigma_{\epsilon,1}, \dots, \Sigma_{\epsilon,k}) \in (\mathbb{R}^{L \times L})^k$. This regularization step ensures that all diagonal elements of $D_{\epsilon,l}$ and therefore all eigenvalues of $\Sigma_{\epsilon,l}$ are strictly positive which makes both matrices always invertible. Additionally, the condition of $\Sigma_{\epsilon,l}$ is always smaller than or equal to the one of Σ_l .

With the regularization, the volume regularizer for the segments becomes

$$\log \det \Sigma_{\epsilon,l} = \log \prod_{r=1}^L \max \{ \sigma_{l,r}^2, \epsilon^2 \}. \quad (5)$$

Since we aim to minimize the objective function, the algorithm tries to make $\det \Sigma_{\epsilon,l}$ small by reducing its eigenvalues and hence the standard deviations of the feature distribution. However, once we have $\sigma_{l,r} \leq \epsilon$ for all $r \in \{1, \dots, L\}$, we cannot improve the objective function values further by adjusting these variables because in this case we obtain with Eq. (5)

$$\log \det \Sigma_{\epsilon,l} = \log \epsilon^{2L}.$$

Consequently, ϵ sets the minimum volume the spectral cluster of a segment can have.

During our studies, we found an article about human face detection [26]. The authors model the distributions of the images also with Gaussian distributions and derive a distribution-dependent distance that is similar to our indicator function in Eq. (3). However, while they derive the mean and covariance from training data, they do not use the square root in their distance function and do not regularize the covariance matrix.

III. OPTIMIZATION

In this section, we describe how the objective function is optimized with respect to its parameters. We use an alternating minimization approach. In the following, we first give information about the overall optimization process, before we describe the subsequent steps. These steps are the parameter initialization (cf. Section III-A), the optimization over μ_l and Σ_l for all $l \in \{1, \dots, k\}$ (cf. Section III-B) and the optimization over u (cf. Section III-C). The section ends with an explanation of the used stopping criterion in Section III-D.

As mentioned in Section II-B2, we have to deal with the lack of a closed form solution for μ_l and Σ_l and the non-differentiability of the square root at 0. We regularize the square root by adding a small constant $\eta > 0$ to solve the latter problem. The resulting regularized indicator function for segment $l \in \{1, \dots, k\}$ and $(i, j) \in \mathcal{N}$ for our discretized objective function can be defined as

$$f_{\eta,l}(i, j; \mu_l, \Sigma_l) := \sqrt{(g^{i,j} - \mu_l)^T \Sigma_l^{-1} (g^{i,j} - \mu_l) + \eta} + \log \det \Sigma_l, \quad (6)$$

with $\mu_l \in \mathbb{R}^L$ and $\Sigma_l \in \mathbb{R}^{L \times L}$ being positive definite but necessarily symmetric. Furthermore, define $f_{\eta,l}^{i,j}(\mu_l, \Sigma_l) := f_{\eta,l}(i, j; \mu_l, \Sigma_l)$ and $u_l^{i,j} := u_l(i, j)$ for $(i, j) \in \mathcal{N}$ and $l \in \{1, \dots, k\}$ and $u^{i,j} := (u_1^{i,j}, \dots, u_k^{i,j})^T \in \mathbb{K}^k$. Then, we can define the discretized objective function (cf. Eqs. (2) and (6)) as

$$E(u, \mu, \Sigma) := \sum_{l=1}^k \sum_{i=1}^H \sum_{j=1}^W u_l^{i,j} f_{\eta,l}^{i,j}(\mu_l, \Sigma_l) + \lambda |u|_{\text{BV}}, \quad (7)$$

with $u = (u^{i,j})_{\substack{i=1,\dots,H, \\ j=1,\dots,W}} \in (\mathbb{K}^k)^{H \times W}$, $\mu = (\mu_1, \dots, \mu_k) \in (\mathbb{R}^L)^k$ and $\Sigma = (\Sigma_1, \dots, \Sigma_k) \in (\mathbb{R}^{L \times L})^k$ with Σ_l being positive definite, but not necessarily symmetric, for all $l \in \{1, \dots, k\}$. As mentioned, optimization is done alternatingly. Given initial estimates for u , μ and Σ as described in Section III-A, we compute the indicator values of our indicator function which implies an update of μ and Σ using u as described in Section III-B and enables us to update u afterwards following the procedure described in Section III-C. We alternate between these two steps of computing the indicator values (updating μ and Σ) and updating u until the stopping criterion described in Section III-D is met or a maximum number of iterations is reached. Furthermore, we perform a hard assignment in each iteration after updating u . That is, although we allow $u^{i,j}$ to take values within \mathbb{K}^k , we project it back onto one of the vertices of the simplex by thresholding. Concretely, we compute

$$c^{i,j} := \min \left\{ \arg \max_{l=1,\dots,k} \{ u_l^{i,j} \} \right\} \in \{1, \dots, k\}, \quad (8)$$

as the new segment label of pixel $(i, j) \in \mathcal{N}$ and set $u^{i,j}$ to the resulting one-hot encoding for that pixel:

$$u^{i,j} := (\delta_{c^{i,j},1}, \delta_{c^{i,j},2}, \dots, \delta_{c^{i,j},k})^T \in \{0, 1\}^k \cap \mathbb{K}^k, \quad (9)$$

where δ_{rs} for $r, s \in \{1, \dots, k\}$ is the Kronecker delta. Thus, outside of Section III-C we assume that $u^{i,j} \in \{0, 1\}^k \cap \mathbb{K}^k$ for

each pixel $(i, j) \in \mathcal{N}$, i.e., $u^{i,j}$ lies on one of the vertices of the unit simplex. The method is summarized in Algorithm 1.

Algorithm 1: Optimization of objective function

Input: Hyperspectral image $\tilde{g}: \mathcal{N} \rightarrow \tilde{V}$, $\lambda > 0$, $\epsilon > 0$, $\eta > 0$;

Result: One-hot encoding of segmentation in u ;

Dimensionality reduction: Apply MNF to \tilde{g} . (cf. Section II-B1);

Initialization: Initialize $u \in (\{0, 1\}^k \cap \mathbb{K}^k)^{H \times W}$, $\mu \in (\mathbb{R}^L)^k$, $\Sigma \in (\mathbb{R}^{L \times L})^k$ (cf. Section III-A). Regularize Σ with ϵ (cf. Section II-B2);

while maximum number of iterations not reached **and** stopping criterion (cf. Section III-D) not met **do**

 Update μ and Σ and compute indicator values with Σ_ϵ (cf. Section III-B);

 Update u (cf. Section III-C);

 Threshold u (cf. Eqs. (8) and (9));

end

A. Initialization

After normalization of the data and application of the MNF to reduce dimensionality and noise, we initialize u as well as μ and Σ by applying the k -means algorithm. Concretely, k -means returns a pixel labeling such that we have a class label $c \in \{1, \dots, k\}$ for each pixel. These class labels can be translated into one-hot encodings $(\delta_{c1}, \delta_{c2}, \dots, \delta_{ck})^T \in \{0, 1\}^k \cap \mathbb{K}^k$ as in Eq. (9). By rearranging the one-hot encodings according to the pixel positions given by \mathcal{N} , we obtain an initial guess for u that lies on one of the vertices of $(\mathbb{K}^k)^{H \times W}$. This labeling from k -means is also used to compute initial values for μ and Σ as empirical means and empirical covariance matrices of the segments according to the formulas given in Eqs. (12) and (13). The covariance matrices are then regularized using ϵ as described before in Section II-B2.

B. Optimization of mean and covariance

As mentioned in Section II-B2, the fact that μ_l and Σ_l are present inside a square root prevented us from deriving a closed form solution for these quantities. In the following, we describe a simple fixed point iteration scheme to optimize over these parameters efficiently. To this end, we define the function

$$h^{i,j}(\mu_l, \Sigma_l) := \sqrt{(g^{i,j} - \mu_l)^T \Sigma_l^{-1} (g^{i,j} - \mu_l) + \eta},$$

for $(i, j) \in \mathcal{N}$ where $\mu_l \in \mathbb{R}^L$ and $\Sigma_l \in \mathbb{R}^{L \times L}$ is positive definite. Then, for every $l \in \{1, \dots, k\}$, we obtain for the

gradient of E (cf. Eq. (7)) with respect to μ_l and Σ_l

$$\partial_{\mu_l} E(u, \mu, \Sigma) = \sum_{i=1}^H \sum_{j=1}^W \frac{u_l^{i,j}}{h^{i,j}(\mu_l, \Sigma_l)} \Sigma_l^{-1} (\mu_l - g^{i,j}),$$

$$\begin{aligned} \partial_{\Sigma_l} E(u, \mu, \Sigma) = & - \sum_{i=1}^H \sum_{j=1}^W \frac{u_l^{i,j}}{2h^{i,j}(\mu_l, \Sigma_l)} \Sigma_l^{-1} (g^{i,j} - \mu_l) (g^{i,j} - \mu_l)^T \Sigma_l^{-1} \\ & + \sum_{i=1}^H \sum_{j=1}^W u_l^{i,j} \Sigma_l^{-1}. \end{aligned}$$

Please note that the formulations of the derivatives take into account that we evaluate E only at positive definite matrices Σ that are also symmetric. For general positive definite matrices, the derivatives deviate from the formulations above. To compute $\partial_{\Sigma_l} E(u, \mu, \Sigma)$, we used that $\partial_{\Sigma_l} \log \det \Sigma_l = \Sigma_l^{-1}$ and that $\partial_{\Sigma_l} b^T \Sigma_l^{-1} b = -\Sigma_l^{-1} b b^T \Sigma_l^{-1}$ for $b \in \mathbb{R}^L$ [27]. Setting the gradients to 0 and reformulating them yields

$$\begin{aligned} \mu_l &= \frac{\sum_{i=1}^H \sum_{j=1}^W \frac{u_l^{i,j}}{h^{i,j}(\mu_l, \Sigma_l)} g^{i,j}}{\sum_{i=1}^H \sum_{j=1}^W \frac{u_l^{i,j}}{h^{i,j}(\mu_l, \Sigma_l)}}, \\ \Sigma_l &= \frac{\sum_{i=1}^H \sum_{j=1}^W \frac{u_l^{i,j}}{2h^{i,j}(\mu_l, \Sigma_l)} (g^{i,j} - \mu_l) (g^{i,j} - \mu_l)^T}{\sum_{i=1}^H \sum_{j=1}^W u_l^{i,j}}. \end{aligned}$$

Since in both cases both sides of the equation depend on μ_l and Σ_l , respectively, we use these expressions to define a fixed point iteration scheme with update rules for $m \in \mathbb{N}_0$ given in Eqs. (10) and (11). Please note that on the left hand side of Eq. (11) we have the *unregularized* covariance matrix. It has to be regularized with an $\epsilon > 0$ as introduced in Section II-B2 by projecting it onto the admissible set of positive definite matrices to ensure invertibility before the next step of the fixed point iteration can be performed.

One can motivate the iteration scheme for μ_l geometrically: find a mean spectrum μ_l that lies within the dense region of the feature distribution by iteratively reducing the influence of points that are far away. Start with an initial estimate, compute the distances of all spectra in the segment to the mean, and use the reciprocal distances as weights to compute a new weighted mean. Repeat the procedure until convergence. This drags μ_l inside the dense region by reducing the influence of more distant spectra. Eq. (10) shows clearly the same structure as the geometric motivation. In the numerator, $u_l^{i,j}$ defines the segment affiliation of each pixel and decides which pixels have to contribute to the mean of segment l . The fraction has the distance of the pixel at (i, j) to the current mean as its denominator, given by $h^{i,j}(\mu_l^{(m)}, \Sigma_{\epsilon,l}^{(m)})$. The fraction is used to weight its spectrum $g^{i,j}$ in the new iterate for μ_l . The denominator of the outer fraction normalizes the weights to sum up to 1.

As initial estimates for the first outer iteration of Algorithm 1, we propose to use the empirical mean and empirical

$$\mu_l^{(m+1)} = \frac{\sum_{i=1}^H \sum_{j=1}^W \frac{u_l^{i,j}}{h^{i,j}(\mu_l^{(m)}, \Sigma_{\epsilon,l}^{(m)})} g^{i,j}}{\sum_{i=1}^H \sum_{j=1}^W \frac{u_l^{i,j}}{h^{i,j}(\mu_l^{(m)}, \Sigma_{\epsilon,l}^{(m)})}}, \quad (10)$$

$$\Sigma_l^{(m+1)} = \frac{\sum_{i=1}^H \sum_{j=1}^W \frac{u_l^{i,j}}{2h^{i,j}(\mu_l^{(m)}, \Sigma_{\epsilon,l}^{(m)})} (g^{i,j} - \mu_l^{(m+1)}) (g^{i,j} - \mu_l^{(m+1)})^T}{\sum_{i=1}^H \sum_{j=1}^W u_l^{i,j}} \quad (11)$$

covariance:

$$\mu_l^{(0)} = \frac{\sum_{i=1}^H \sum_{j=1}^W u_l^{i,j} g^{i,j}}{\sum_{i=1}^H \sum_{j=1}^W u_l^{i,j}}, \quad (12)$$

$$\Sigma_l^{(0)} = \frac{\sum_{i=1}^H \sum_{j=1}^W u_l^{i,j} (g^{i,j} - \mu_l^{(0)}) (g^{i,j} - \mu_l^{(0)})^T}{\sum_{i=1}^H \sum_{j=1}^W u_l^{i,j} - 1}. \quad (13)$$

Once the fixed point iteration scheme was applied for the first time, i.e., in the first outer iteration, its output can be used as an initial guess for the next application in the following outer iteration. Please note as above that Eq. (13) yields the *unregularized* $\Sigma_l^{(0)}$ that needs to be regularized to obtain $\Sigma_{\epsilon,l}^{(0)}$.

We stop the fixed point iteration once a maximum number of iterations is reached or the expression

$$\left\| \mu_l^{(m+1)} - \mu_l^{(m)} \right\|_2 + \left\| D_{\epsilon,l}^{(m+1)} - D_{\epsilon,l}^{(m)} \right\|_F + \left\| U_l^{(m+1)} - U_l^{(m)} \right\|_F$$

is below a certain threshold. Here, the matrices $D_{\epsilon,l}^{(m)}$ and $U_l^{(m)}$ are given by the eigenvalue decomposition $\Sigma_{\epsilon,l}^{(m)} = U_l^{(m)} D_{\epsilon,l}^{(m)} (U_l^{(m)})^T$.

C. Optimization of labeling function

We use the primal-dual hybrid gradient (PDHG) method proposed by Chambolle and Pock [28] to optimize E with respect to u . It is especially suitable to solve convex optimization problems of the form

$$\min_{u \in \mathbb{R}^n} F(u) + G(Au),$$

for closed, proper and convex functions $F: \mathbb{R}^n \rightarrow \mathbb{R}$ and $G: \mathbb{R}^d \rightarrow \mathbb{R}$, as well as a linear function $A: \mathbb{R}^n \rightarrow \mathbb{R}^d$. In our case, F is given as the data term of our objective functional (cf. Eq. (7)), i.e., the sum of the indicator values multiplied by the values of u and summed over all segments plus the convex indicator function of the admissible set $(\mathbb{K}^k)^{H \times W}$ that outputs ∞ if u is outside of $(\mathbb{K}^k)^{H \times W}$ and 0 otherwise. The linear function A is the forward finite differences operator with step size $h = 1/(\max(H, W) - 1)$ that approximates for each pixel $(i, j) \in \mathcal{N}$ fulfilling $i \neq H$ and $j \neq W$ the class-wise gradient $\nabla u(i, j)$ by comparing $u(i, j)$ to $u(i, j+1)$ and $u(i+1, j)$, respectively. At boundary pixels where forward finite differences point outside of the domain, we set the derivative in the corresponding direction to 0. The function G computes the sum over the pixel-wise Euclidean norm of

the pixel-wise gradient of u which equals the discrete total variation of u .

Let $\tau > 0$ and $\sigma > 0$. The PDHG algorithm is given in Algorithm 2. For $(i, j) \in \mathcal{N}$ define $f_\eta^{i,j} :=$

Algorithm 2: primal-dual hybrid gradient method

Input: $\tau > 0, \sigma > 0, u^{(0)} \in \mathbb{R}^n$;

Result: $u^{(m+1)} \in \mathbb{R}^n$;

Initialization: $\bar{u}^{(0)} = u^{(0)} \in \mathbb{R}^n, p^{(0)} \in \mathbb{R}^d$ and

$\theta \in [0, 1]$;

while maximum number of iterations not reached **and**

$\|u^{(m+1)} - u^{(m)}\|_\infty \geq t$ for a threshold $t > 0$ **do**

$p^{(m+1)} = \text{prox}_{\sigma G^*}(p^{(m)} + \sigma A \bar{u}^{(m)})$;

$u^{(m+1)} = \text{prox}_{\tau F}(u^{(m)} - \tau A^T p^{(m+1)})$;

$\bar{u}^{(m+1)} = u^{(m+1)} + \theta (u^{(m+1)} - u^{(m)})$;

end

$(f_{\eta,1}^{i,j}(\mu_1, \Sigma_1), \dots, f_{\eta,k}^{i,j}(\mu_k, \Sigma_k))^T \in \mathbb{R}^k$. Furthermore, let $f_\eta := (f_{\eta}^{i,j})_{i=1, \dots, H, j=1, \dots, W} \in (\mathbb{R}^k)^{H \times W}$ be the tensor containing the indicator values of all pixels. Then, the involved proximal mappings can be derived in a closed form, i.e.,

$$\text{prox}_{\tau F}(u) = P_{\mathbb{K}^k} \left(u - \frac{\tau}{\lambda} f_\eta \right),$$

$$\text{prox}_{\sigma G^*}(p) = P_{\overline{B_2}}(p),$$

where $P_{\mathbb{K}^k}$ is the pixel-wise projection onto the unit simplex \mathbb{K}^k and $P_{\overline{B_2}}$ the pixel-wise projection onto the closed unit ball with respect to the Euclidean norm in two dimensions. An efficient algorithm to compute $P_{\mathbb{K}^k}$ can be found in [29].

D. Stopping criterion

We stop the outer iteration in Algorithm 1 once the expression

$$\sum_{l=1}^k \frac{\sum_{i=1}^H \sum_{j=1}^W (u^{(m)})_l^{i,j}}{HW} \left\| \mu_l^{(m)} - \mu_l^{(m-1)} \right\|_\infty < t,$$

with $m \in \mathbb{N}$ being the current iteration, is true for a threshold $t > 0$ or when $m = m_{\max}$ for a constant $m_{\max} \in \mathbb{N}$. The idea is to stop the iteration when the resulting segmentation, i.e., u after thresholding, does not change substantially anymore or when a maximum number of iterations is reached. We use the mean spectra of the segments to measure the change in u . The weighting by the cardinality of the segments is introduced to reduce the influence of changes of labels in segments with only a few pixels as in such cases the influence of a single

pixel on the mean spectrum is stronger than in segments with many pixels. Therefore, using such a weighting, it is avoided that only a few pixels in small segments keep the algorithm iterating because their labels are alternating between two classes.

IV. NUMERICAL RESULTS

Tests of our model were performed on four publicly available datasets from the remote sensing community: Indian Pines (IP), Kennedy Space Center (KSC), Pavia University (PU) and Salinas (SA).

A. Datasets

Brief descriptions of the datasets¹ that were used for evaluation are given in the following:

- 1) *Indian Pines*: this dataset, that was acquired with an AVIRIS sensor in north-western Indiana, has a size of 145×145 pixels and contains 220 spectral channels per pixel. The ground truth divides the image into 16 land cover classes. We use the version where the water absorption bands were discarded, resulting in 200 channels per pixel.
- 2) *Kennedy Space Center*: this dataset was acquired with an AVIRIS sensor over the Kennedy Space Center in Florida. The 512×614 pixels contain 224 channels each. The water absorption and noisy channels were discarded, resulting in 176 channels for our analysis. The ground truth describes 13 classes of land cover types.
- 3) *Pavia University*: the data was acquired with a ROSIS sensor over Pavia in northern Italy. There are 103 clean channels for each of the 610×340 pixels. The ground truth distinguishes between 9 land cover types.
- 4) *Salinas*: the last dataset is again an AVIRIS dataset, acquired over the Salinas Valley in California. It is built of 512×217 pixels with 224 channels each. The ground truth divides the data into 16 classes of land cover types. We test on the version of the dataset where 20 water absorption bands were removed.

B. Assessment of segmentations

To assess our obtained segmentations, we compare the segmentation map to the corresponding ground truth of the respective dataset. Since the labeling of the segments in the segmentation map not necessarily corresponds to the ground truth labels, we find the best matching of the labels by computing the confusion matrix and letting the Hungarian algorithm [30] find the permutation that leads to the highest values on the diagonal and therefore the best matching in this sense. Based on this confusion matrix, we compute the overall accuracy (OA), the average class accuracy (AA) and the kappa coefficient (KC) [31]. OA is defined as the fraction of correctly classified pixels, AA describes the average over the class accuracies and KC measures the agreement of two classifications taking into account a possible agreement by chance.

¹Datasets available under http://www.ehu.es/ccwintco/index.php?title=Hyperspectral_Remote_Sensing_Scenes

C. Experiments

Before applying our segmentation framework, we normalize the raw data to have intensity values in each channel and for each pixel in $[0, 1]$ by subtracting the minimum intensity and dividing by the resulting maximum. Since this transformation is linear, it only changes the value range but not the structure of the data. The choice of the parameters of our model is given in Table I. Only the parameters λ , ϵ and the number of components L are chosen image-dependent by picking the parameter setting that gave the highest OA after grid search.

We compare our model with the sequential spectral clustering approach combined with the RBF kernel (SSC) [15] and a MS based segmentation functional equipped with a nonlocal total variation regularization (NLTV) [14]. We chose these two methods as they are current state-of-the-art methods for unsupervised hyperspectral segmentation. In particular, NLTV and our framework are both based on the MS segmentation functional. All methods were given the number of segments k as prior information. In principle, the MNF transform we use as dimensionality and noise reduction technique could also be applied as a preprocessing step in the competing methods. However, as we had no access to the corresponding implementations, we could not do that, but use their tabulated scores from literature instead. The achieved scores are given in

IP				KSC			
k	λ	ϵ	L	k	λ	ϵ	L
16	0.15	0.3	8	13	0.0005	0.5	6
PU				SA			
k	λ	ϵ	L	k	λ	ϵ	L
9	0.02	0.3	5	16	0.12	0.2	7

η	
10^{-2}	

Stopping thresholds		
Outer iterations	PDHG iterations	Fixed point iterations
10^{-6}	10^{-6}	10^{-5}

Maximum number of iterations		
Outer iterations	PDHG iterations	Fixed point iterations
20	1000	20

Table I: Chosen parameters for our model. The number of segments k is given by the ground truth.

Table II. Our segmentation framework performs significantly better than the other two approaches on the datasets IP, KSC and SA. In particular, the performance boosts on IP and KSC are substantial. Only on the PU dataset SSC beats our approach. However, our algorithm still achieves a considerable score. Notably, the performance boost on IP, KSC and SA by our method compared to SSC and NLTV is much larger than the difference in the scores of SSC and our method on PU. Figs. 2 to 5 show the ground truths of the test datasets and the segmentations found by our method. The colors used for visualization are adapted from [32]. The segment boundaries given by the ground truths are laid over the full segmentations in Figs. 2b, 3b, 4b and 5b. Pixels that are unlabeled in the ground truth are marked in black in Figs. 2c, 3c, 4c and 5c. One can see that we obtain homogeneous and connected areas. Notably, the rose and the gray segment in the upper left part

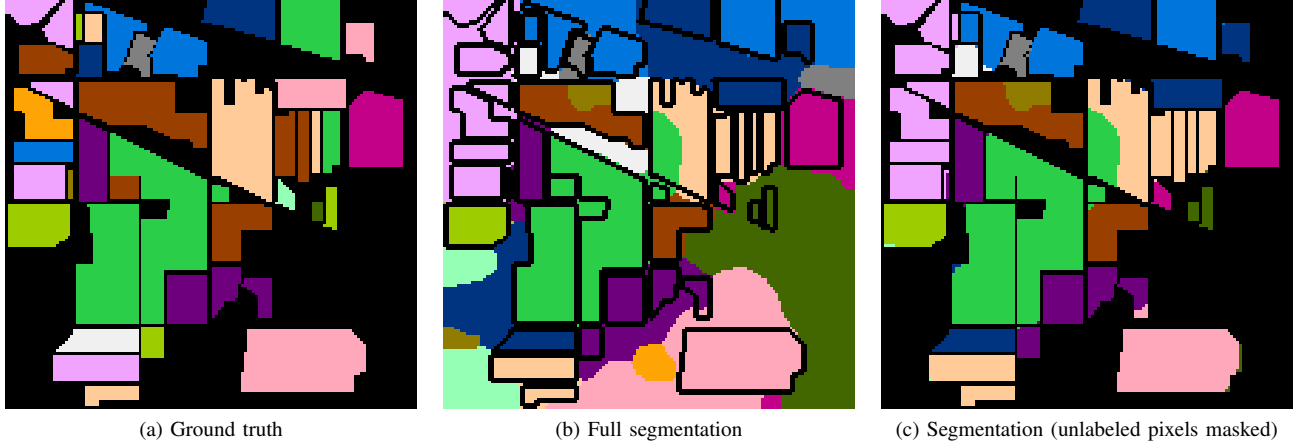


Figure 2: Ground truth and segmentation of IP produced by our method.

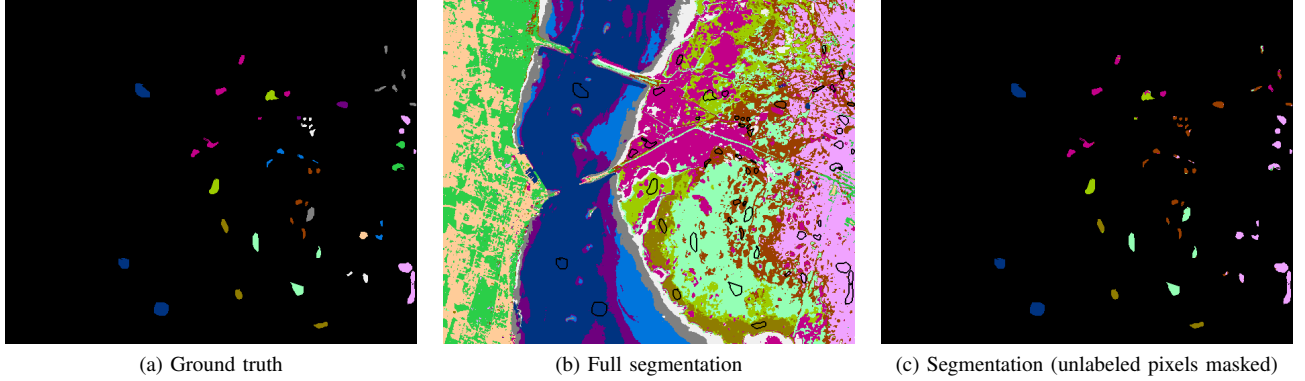


Figure 3: Ground truth and segmentation of KSC produced by our method.

		NLTV	SSC	Ours
IP	OA	42.4 %	42.9 %	70.1 %
	AA	-	-	59.6 %
	KC	-	36.5 %	66.3 %
KSC	OA	41.5 %	-	71.6 %
	AA	-	-	53.0 %
	KC	-	-	68.0 %
PU	OA	44.0 %	68.2 %	61.5 %
	AA	-	-	59.6 %
	KC	-	62.2 %	53.4 %
SA	OA	-	81.8 %	89.0 %
	AA	-	-	76.3 %
	KC	-	79.8 %	87.8 %

Table II: Scores of the methods NLTV and SSC compared to our framework. The best scores are printed in bold. NLTV was not tested on SA and SSC was not tested on KSC. Only the OA score is given for NLTV in [14]. The AA score for SSC is not reported in [15].

of the SA dataset (cf. Fig. 5) describe the classes *vineyard untrained* and *grapes untrained*. Both classes show a high spectral similarity. Many approaches have problems to separate these two classes, resulting in segments that are usually completely mixed up. Our segmentation framework, however, separates these two segments very well. Also IP contains many segments that are spectrally similar. Nevertheless, our method

achieves a good score on the dataset. In case of IP, KSC and SA our method uses some segments exclusively for unlabeled pixels, which results in less classes in the segmentations within the labeled pixels than are actually present in the ground truths within these pixels. As a consequence, segments that are separated in the ground truths are merged in the segmentation as the number of segments k is fixed.

V. CONCLUSION

In this article, we presented a new unsupervised segmentation framework for hyperspectral images based on the MS segmentation functional equipped with a novel robust distribution-dependent indicator function that was designed to handle the spectral variability of HSI data. The method has proven to be suitable for the task at hand by achieving considerable scores on all four test dataset. In particular, it beat the competitors on three of the four datasets with substantially higher accuracies. The method was even able to separate clusters with a high spectral similarity and could handle the spectral variability adequately. Moreover, we proposed an efficient fixed point iteration scheme to optimize the objective function with respect to the parameters for which, to the best of our knowledge, no closed form solution is available.

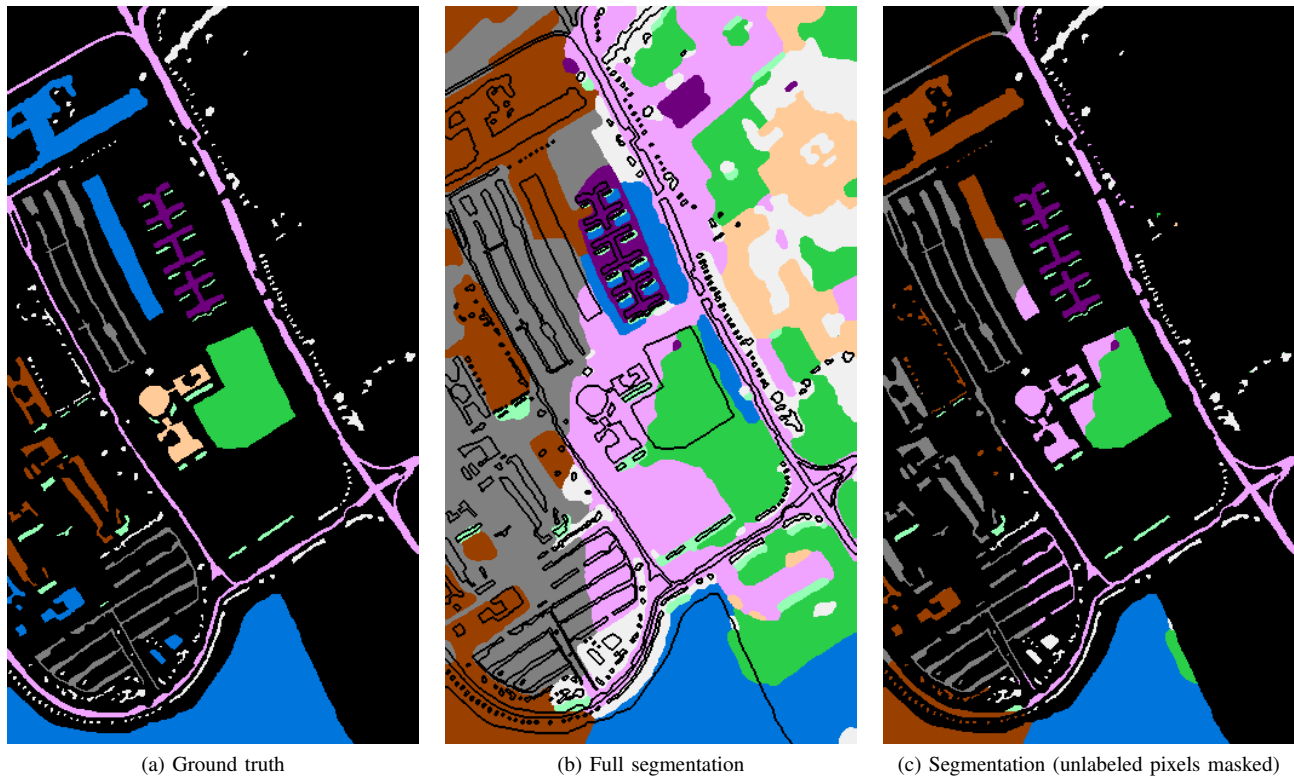


Figure 4: Ground truth and segmentation of PU produced by our method.

As the next step, we will focus on the noise estimation scheme for the MNF transform, which currently is rather simplistic. We believe that by replacing it by a scheme that uses assumptions that are more realistic and suitable for HSI data, the segmentation results can be further improved. Moreover, the estimation of the noise covariance matrix was done globally. We plan to apply the MNF transform only locally on adaptive neighborhoods with the goal to preserve the segment boundaries, similar to the approach in [33]. These adaptive neighborhoods can be either obtained by applying a superpixel segmentation method or by running our segmentation framework once on the data and rerunning it after applying the MNF transform on each of the segments found in the first run separately.

ACKNOWLEDGMENTS

This work was funded by the Deutsche Forschungsgemeinschaft (DFG, German Research Foundation) – 333849990/GRK2379 (IRTG Modern Inverse Problems).

The research of Chandrajit Bajaj was additionally supported in part by the Peter O'Donnell Foundation.

REFERENCES

- [1] J. P. Kerekes and J. R. Schott, *Hyperspectral Imaging Systems*. John Wiley & Sons, Ltd, 2007, ch. 2, pp. 17–45. [Online]. Available: <https://onlinelibrary.wiley.com/doi/abs/10.1002/9780470124628.ch2>
- [2] M. E. Paoletti, J. M. Haut, J. Plaza, and A. Plaza, “Deep learning classifiers for hyperspectral imaging: A review,” *ISPRS Journal of Photogrammetry and Remote Sensing*, vol. 158, pp. 279–317, Dec. 2019.
- [3] P. R. Griffiths and J. A. de Haseth, *Introduction to Vibrational Spectroscopy*, 2nd ed. John Wiley & Sons, Ltd, Apr. 2007, ch. 1, pp. 1–18. [Online]. Available: <https://onlinelibrary.wiley.com/doi/abs/10.1002/9780470106310.ch1>
- [4] J. M. Bioucas-Dias, A. Plaza, N. Dobigeon, M. Parente, Q. Du, P. Gader, and J. Chanussot, “Hyperspectral Unmixing Overview: Geometrical, Statistical, and Sparse Regression-Based Approaches,” *IEEE Journal of Selected Topics in Applied Earth Observations and Remote Sensing*, vol. 5, no. 2, pp. 354–379, April 2012.
- [5] A. Camacho, C. V. Correa, and H. Arguello, “An analysis of spectral variability in hyperspectral imagery: a case study of stressed oil palm detection in colombia,” *International Journal of Remote Sensing*, vol. 40, no. 19, pp. 7603–7623, mar 2019. [Online]. Available: <https://doi.org/10.1080/01431161.2019.1595210>
- [6] L. Gao, J. Li, M. Khodadadzadeh, A. Plaza, B. Zhang, Z. He, and H. Yan, “Subspace-based support vector machines for hyperspectral image classification,” *IEEE Geoscience and Remote Sensing Letters*, vol. 12, no. 2, pp. 349–353, Feb. 2015.
- [7] M. Cholewa and P. Glomb, “Two stage SVM classification for hyperspectral data,” in *Proceedings of the 5th International Conference on Pattern Recognition Applications and Methods*, INSTICC. SciTePress, 2016, pp. 387–391.
- [8] S. K. Roy, G. Krishna, S. R. Dubey, and B. B. Chaudhuri, “HybridSN: Exploring 3-d-2-d CNN feature hierarchy for hyperspectral image classification,” *IEEE Geoscience and Remote Sensing Letters*, vol. 17, no. 2, pp. 277–281, Feb. 2020.
- [9] S. K. Roy, S. Manna, T. Song, and L. Bruzzone, “Attention-based adaptive spectral-spatial kernel ResNet for hyperspectral image classification,” *IEEE Transactions on Geoscience and Remote Sensing*, vol. 59, no. 9, pp. 7831–7843, Sep. 2021.
- [10] Z. Xue, M. Zhang, Y. Liu, and P. Du, “Attention-based second-order pooling network for hyperspectral image classification,” *IEEE Transactions on Geoscience and Remote Sensing*, vol. 59, no. 11, pp. 9600–9615, nov 2021.
- [11] G. F. Hughes, “On the mean accuracy of statistical pattern recognizers,” *IEEE Transactions on Information Theory*, vol. 14, no. 1, pp. 55–63, jan 1968.
- [12] J. A. Richards and X. Jia, *Remote sensing digital image analysis : an introduction*, 4th ed. Berlin: Springer-Verlag Berlin

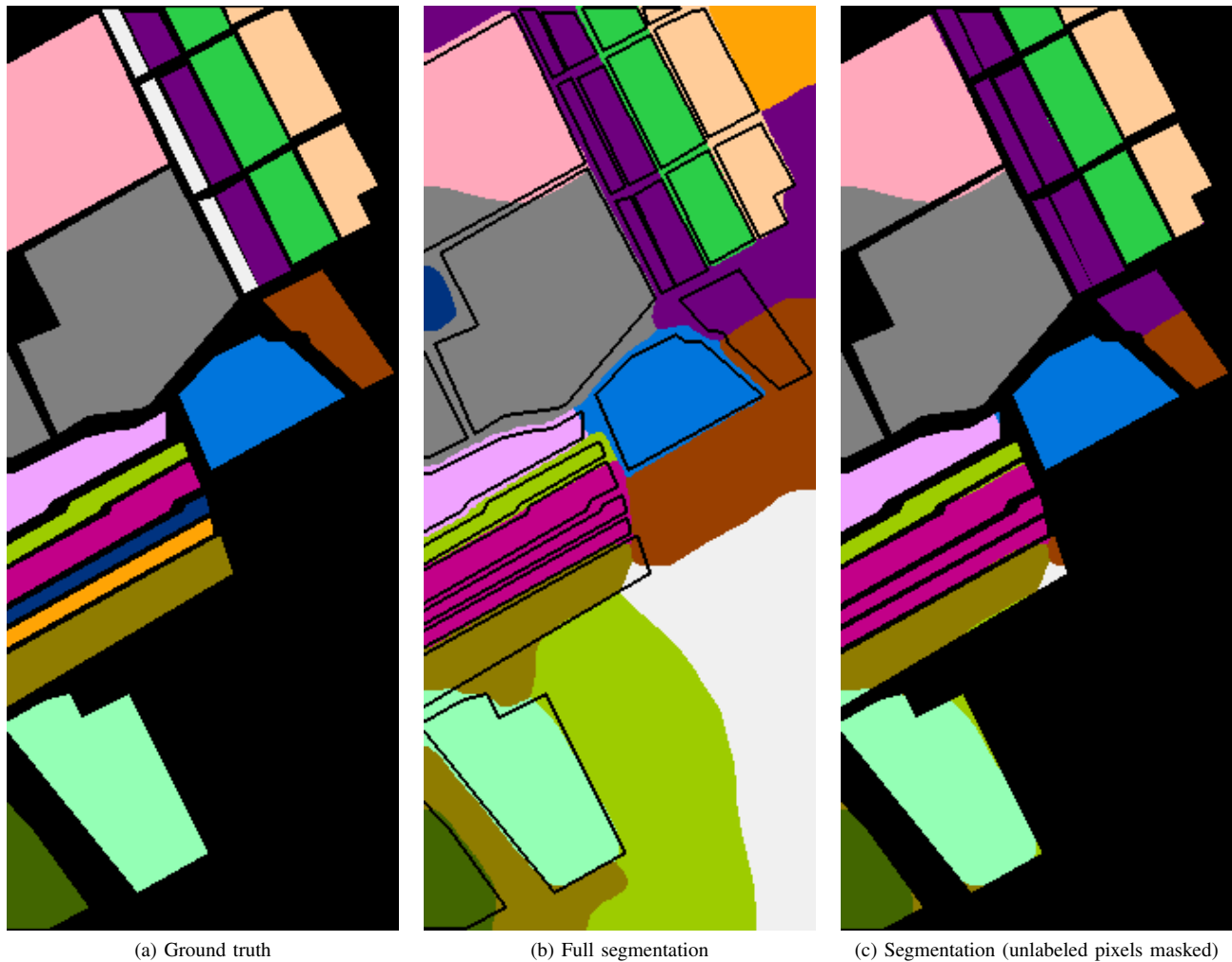


Figure 5: Ground truth and segmentation of SA produced by our method.

- Heidelberg, 2006. [Online]. Available: <https://link.springer.com/book/10.1007/3-540-29711-1>
- [13] M. Ester, H.-P. Kriegel, J. Sander, and X. Xu, "A density-based algorithm for discovering clusters in large spatial databases with noise," in *Proceedings of the Second International Conference on Knowledge Discovery and Data Mining*, ser. KDD'96. AAAI Press, 1996, pp. 226–231.
- [14] W. Zhu, V. Chayes, A. Tiard, S. Sanchez, D. Dahlberg, A. L. Bertozzi, S. Osher, D. Zosso, and D. Kuang, "Unsupervised classification in hyperspectral imagery with nonlocal total variation and primal-dual hybrid gradient algorithm," *IEEE Transactions on Geoscience and Remote Sensing*, vol. 55, no. 5, pp. 2786–2798, May 2017.
- [15] A. Hassanzadeh, A. Kaarna, and T. Kauranne, "Sequential spectral clustering of hyperspectral remote sensing image over bipartite graph," *Applied Soft Computing*, vol. 73, pp. 727–734, Dec. 2018.
- [16] L. Zhang, L. Zhang, B. Du, J. You, and D. Tao, "Hyperspectral image unsupervised classification by robust manifold matrix factorization," *Information Sciences*, vol. 485, pp. 154–169, Jun. 2019.
- [17] D. Mumford and J. Shah, "Optimal approximations by piecewise smooth functions and associated variational problems," *Comm. Pure Appl. Math.*, vol. 42, no. 5, pp. 577–685, 1989.
- [18] C. Zach, D. Gallup, J.-M. Frahm, and M. Niethammer, "Fast global labeling for real-time stereo using multiple plane sweeps," in *VMV*, 2008, pp. 243–252.
- [19] A. A. Green, M. Berman, P. Switzer, and M. D. Craig, "A Transformation for Ordering Multispectral Data in Terms of Image Quality with Implications for Noise Removal," *IEEE Transactions on Geoscience and Remote Sensing*, vol. 26, no. 1, pp. 65–74, Jan. 1988. [Online]. Available: <https://ieeexplore.ieee.org/document/3001>
- [20] K. Pearson, "LIII. on lines and planes of closest fit to systems of points in space," *The London, Edinburgh, and Dublin Philosophical Magazine and Journal of Science*, vol. 2, no. 11, pp. 559–572, nov 1901.
- [21] M. Berman, A. Phatak, and A. Traylen, "Some invariance properties of the minimum noise fraction transform," *Chemometrics and Intelligent Laboratory Systems*, vol. 117, pp. 189–199, Aug. 2012, special Issue Section: Selected Papers from the 1st African-European Conference on Chemometrics, Rabat, Morocco, September 2010 Special Issue Section: Preprocessing methods Special Issue Section: Spectroscopic imaging. [Online]. Available: <http://www.sciencedirect.com/science/article/pii/S0169743912000391>
- [22] J. B. Lee, A. S. Woodyatt, and M. Berman, "Enhancement of high spectral resolution remote-sensing data by a noise-adjusted principal components transform," *IEEE Transactions on Geoscience and Remote Sensing*, vol. 28, no. 3, pp. 295–304, May 1990.
- [23] S. Gupta, S. Mittal, A. Kajdacsy-Balla, R. Bhargava, and C. Bajaj, "A fully automated, faster noise rejection approach to increasing the analytical capability of chemical imaging for digital histopathology," *PLOS ONE*, vol. 14, no. 4, pp. 1–15, Apr. 2019. [Online]. Available: <https://doi.org/10.1371/journal.pone.0205219>
- [24] S. Gupta and C. Bajaj, "A Streaming model for Generalized Rayleigh with extension to Minimum Noise Fraction," in *2019 IEEE International Conference on Big Data (Big Data)*, 2019, pp. 74–83.
- [25] P. C. Mahalanobis, "On the generalized distance in statistics," *Proceedings of the National Institute of Sciences (Calcutta)*, vol. 2, pp. 49–55, 1936.
- [26] K.-K. Sung and T. Poggio, "Example-based learning for view-based human face detection," *IEEE Transactions on Pattern Analysis and Machine Intelligence*, vol. 20, no. 1, pp. 39–51, Jan. 1998.

- [27] K. B. Petersen and M. S. Pedersen, "The Matrix Cookbook," nov 2012, version 20121115. [Online]. Available: <http://www2.compute.dtu.dk/pubdb/pubs/3274-full.html>
- [28] A. Chambolle and T. Pock, "A first-order primal-dual algorithm for convex problems with applications to imaging," *J. Math. Imaging Vision*, vol. 40, no. 1, pp. 120–145, 2011. [Online]. Available: <http://dx.doi.org/10.1007/s10851-010-0251-1>
- [29] W. Wang and M. Á. Carreira-Perpiñán, "Projection onto the probability simplex: An efficient algorithm with a simple proof, and an application," 2013. [Online]. Available: <https://arxiv.org/abs/1309.1541>
- [30] H. W. Kuhn, "The Hungarian method for the assignment problem," *Naval Research Logistics Quarterly*, vol. 2, no. 1-2, pp. 83–97, 1955.
- [31] J. Cohen, "A coefficient of agreement for nominal scales," *Educational and Psychological Measurement*, vol. 20, no. 1, pp. 37–46, 1960. [Online]. Available: <https://doi.org/10.1177/001316446002000104>
- [32] P. Green-Armytage, "A Colour Alphabet and the Limits of Colour Coding," *JAIC - Journal of the International Colour Association*, vol. 5, 2010.
- [33] S. Gupta and C. Bajaj, "Efficient Clustering-Based Noise Covariance Estimation for Maximum Noise Fraction," in *Computer Vision, Pattern Recognition, Image Processing, and Graphics*, R. Rameshan, C. Arora, and S. Dutta Roy, Eds. Singapore: Springer Singapore, 2018, pp. 232–244.
- [34] O. Tange, "GNU Parallel 20200922 ('Ginsburg')," Sep. 2020, GNU Parallel is a general parallelizer to run multiple serial command line programs in parallel without changing them. [Online]. Available: <https://doi.org/10.5281/zenodo.4045386>